Sensors and Materials, Vol. 38, No. 9 (2026) 5229–5242
MYU Tokyo

S & M 4620

Early Prediction of Skin Pressure Ulcers Through an Ordinary Camera: Hyperspectral Images and Generative Learning Approaches

Yenming J. Chen,[1,2†] Kao-Shing Hwang,[2,3†] Sheng-Yiao Lin,[4]
Chin-Lan Chen,[5*] and Wen-Hsien Ho[2,6,7,8,9**]

[1]Department of Information Management, National Kaohsiung University of Science and Technology, Kaohsiung 824005, Taiwan
[2]Department of Healthcare Administration and Medical Informatics, Kaohsiung Medical University, Kaohsiung 807378, Taiwan
[3]Department of Electrical Engineering, National Sun Yat-Sen University, Kaohsiung 804201, Taiwan
[4]Department of Dermatology, Kaohsiung Medical University Hospital, Kaohsiung 807378, Taiwan
[5]Department of Family Medicine, Yuan's General Hospital, Kaohsiung 802635, Taiwan
[6]Department of Fragrance and Cosmetic Science, Kaohsiung Medical University, Kaohsiung 807378, Taiwan
[7]Department of Medical Research, Kaohsiung Medical University Hospital, Kaohsiung 807378, Taiwan
[8]Precision Sports Medicine and Health Promotion Center, Kaohsiung Medical University, Kaohsiung 807378, Taiwan
[9]College of Professional Studies, National Pingtung University of Science and Technology, Pingtung 912301, Taiwan

(Received March 4, 2026; accepted June 9, 2026)

Keywords: pressure ulcers, skin tissue, hyperspectral imaging (HSI), appearance optical property (AOP), double-end generative matching (DGM), Monte Carlo method for multilayered media (MCML), chromophores, bio-optical model (BOM)

Pressure ulcers are a significant concern in nursing care. However, preventing pressure ulcers often relies solely on visual assessments of skin tissue. For example, changes in skin color can be due to factors such as oxygen deficiency and external effects. However, the internal composition of skin may vary significantly despite appearing identical on the surface. Given that skin tissue is semitransparent to light, long-wavelength colors such as red and yellow penetrate deep into the skin tissue and reflect at different depths. This phenomenon provides spectral images representing the superimposed state of the tissue layers. These overlapped reflection spectra are undetectable by the naked eye and can only be identified by hyperspectral imaging. In this study, we introduce the double-end generative matching technique to address the insensitivity in detecting skin abnormalities by sight alone. Unlike traditional methods in which RGB images are used, we believe that the correct estimation of hemoglobins must retrieve the complete composition of chromophores through the reflected hyperspectral lights within layers of skin. This method uses a Monte Carlo method for multilayered media (MCML) simulations to produce non-

*Corresponding author: e-mail: 900pchinlan@gmail.com
**Corresponding author: e-mail: whho@kmu.edu.tw
†Equal contributors
https://doi.org/10.18494/SAM6323

ISSN 0914-4935

overlapping surface spectra for specified damaged tissue, with authentic images providing feedback to refine the simulated skin model's accuracy. We generate a vast training dataset for bidirectional training with the trained optical model, and we can accurately predict the concentration of skin chromophores to identify subtle differences that may not be visible to the naked eye. This method enables the identification of areas in the dermis with low levels of oxygenated hemoglobin (Hb) and abnormal water content. From an arbitrary picture, our model decomposes a complete set of contents into skin layers. Two chemical substances are used to predict ulcers, and the rest of the paper will be used to validate the consistency of our estimations. Our results show significant consistency between our prediction and the ground truth.

1. Introduction

In nursing, the risk of pressure ulcers is assessed using widely recognized tools such as the Braden Scale, Norton Scale, Gosnell Scale, and Waterlow Scale. Because of the prolonged immobility and sustained pressure on bedridden patients, local tissue hypoxia or cell damage often leads to the development of pressure ulcers. Since internal pathological changes of the skin are difficult to observe directly, once a pressure ulcer develops, it often causes significant discomfort to the patient, and initiating treatment after the symptoms become apparent is usually very late. However, if a digital twin—a virtual representation of the patient—could be used, synchronized with the patient through a computer-based three-dimensional fluid model to reconstruct the circulatory conditions of the patient's entire body and identify high-risk areas, it would significantly save care labor and enhance the quality of care. Therefore, in this study, we aim to tackle the challenge of detecting pressure ulcers before they become visually noticeable by employing hyperspectral imaging (HSI) technology for early detection. This allows for timely warning before the formation of pressure ulcers, preventing damage to skin tissue. This is because HSI is applicable to analyze light reflection and absorption properties at different wavelengths on the skin, detecting changes in blood supply, oxygen saturation, and other physiological parameters in the underlying tissues. Nouvong *et al.*[1] noted that multispectral imaging technology could be used to detect early-stage skin changes due to insufficient local blood supply, which is crucial for preventing and treating pressure ulcers.

In previous studies, several methods were used for detecting early signs of pressure ulcers, including visual inspection, pressure measurement devices, thermal imaging technology, and HSI technology. HSI technology is widely used to differentiate hemoglobin (Hb) from melanin in tissues[2,3] and is applied in monitoring and analyzing skin features such as redness, acne, and moles.[4] It has been demonstrated in previous studies that HSI can reveal the spatial distribution of oxygenated Hb (HbO_2), deoxygenated Hb, and melanin in the skin.[2,5] With changes in spectral reflectance, HSI can further clarify tissue morphological alterations and chromophore-concentration changes associated with skin lesions.[6–8] Wu[9] introduced an innovative HSI system featuring active sequential bandpass illumination integrated into conventional optical instruments. This system utilizes multivariate linear regression to analyze HbO_2 and Hb saturation in animal tissue samples.

Shetty *et al.*[10] used machine learning and convolutional neural networks (CNNs) for the classification of skin lesions. Their research utilizes data augmentation and the k-fold cross-validation technique, significantly enhancing the model's robustness. Compared with other machine-learning algorithms, CNNs demonstrate superior accuracy, with the CNN model used in this study achieving the highest accuracy rate of 95.18%. This high accuracy enables the early identification of seven distinct types of skin diseases, thereby assisting physicians in verification and appropriate treatment. He *et al.*[11] claimed to detect spectral changes in HbO_2 and deoxygenated Hb within skin tissue. Their study involved two experiments on skin tissue beds subjected to occlusive maneuvers of supplying arteries: one utilizing the extensively recognized blood cuff pressure maneuver on the upper arm and the other artificially inducing a transient ischemic condition on facial skin tissue beds by applying digital pressure on the supplying external carotid artery.

Kazune *et al.*[12] used HSI to measure septic patients' microcirculatory oxygenation. Their results indicate that elevating the mean arterial pressure in these patients can effectively improve microcirculatory oxygenation for the majority. Khoobehi *et al.*[13] used HSI to assess relative blood oxygen saturation changes in the eyes and optic nerve heads of cynomolgus monkeys under different eye pressures. Thus, elevated eye pressure leads to reduced oxygen saturation across all structures. Ahmed *et al.*[14] utilized diffuse reflectance spectroscopy to investigate the effects of probe pressure on human skin. The unique composition and morphology of each tissue type, including fingertip, forearm, forehead, neck, and foot, are found to affect the shape, size, intensity, and position of the recorded peak. This finding highlights the tissue-specific response to pressure. Drakaki and Sianoudis.[15] found that the characteristic absorption bands of HbO_2 at 542 and 577 nm are affected by blood-flow occlusion and reactive hyperemia in the arm, leading to changes in spectral reflectance intensity.

On the basis of the findings of the above studies, we develop a method to reconstruct hyperspectral information from standard RGB images obtained using regular cameras to understand the distribution of melanin, HbO_2, and Hb in the skin. Previous studies have revealed the feasibility of using multivariate regression analysis to evaluate the concentrations of melanin and Hb in the skin.[16,17] Independent component analysis was conducted to generate color-distribution maps for melanin and Hb.[18] However, these methods may face limitations regarding the range of parameters in practice. Conversely, diffusion approximation and radiative transfer equation-based auxiliary function methods were used in some studies[19,20] to determine the optical properties of the skin. These methods are theoretically viable but face challenges when applied to heterogeneous skin-tissue models.[21] Regarding this problem, the results of recent studies have shown that optical parameters of skin tissues, such as absorption coefficient (μ_a), scattering coefficient (μ_s), anisotropy factor (g), refractive index (n), and thickness (d), can significantly impact spectral reflectance.[22] Given that light penetration depth is wavelength-dependent and the uneven distribution of blood in the dermis affects the morphology of the reflection spectrum, it is crucial to consider these factors when developing skin optical models.[23]

To overcome the limitations of previous models, in this study, we use the Monte Carlo method for multilayered media (MCML) to simulate the concentrations of various chromophores in the different layers of the skin.[24] This method can be used to simulate light transmission in scattered media within tissues while considering the complexity of the geometric shape and boundary conditions of biological tissues.[25] Furthermore, owing to the advancement in modern computer technology, especially the application of GPU acceleration, MCML computations can be completed within a reasonable time frame.[26] We aimed to develop a dynamic spectral model of skin tissue that allows for the computer-based analysis of real-time imaging to reconstruct the concentration distributions of different chromophores within personal skin tissues. This model also detects changes in oxygenated HbO_2 in arterial vessels in response to pressure, thereby establishing a real-time system for monitoring the skin health status.

2. Methods

2.1 Dataset description and evidence base

We rely on a simulation dataset that couples smartphone photographs with reference reflectance spectra measured by a spectrometer. The simulation dataset provides paired RGB images and reflectance spectra to anchor the forward optical model and to quantify spectral reconstruction error (Sect. 3.2).

For reproducibility, the dataset recorded the following metadata: the number of subjects (N), the number of imaging sessions per subject (T), the number of images per session (K), anatomical sites (e.g., sacrum, and heel), Fitzpatrick skin-type distribution, age and sex distributions, ulcer stage labels (e.g., stage 0 to 4), and time-to-event labels relative to the first visible ulcer sign. In the current pilot study, these values are recorded in the raw data logs and summarized in a dedicated dataset summary table.

The physiological evidence base motivating the chosen chromophore variables follows prior findings that local ischemia and microcirculatory impairment affect dermal oxygenation (HbO_2 and Hb) and that pressure-related edema affects water content, which can precede visible erythema. Hyperspectral and multispectral studies have reported that such chromophore-associated spectral changes can appear before overt skin breakdown, supporting the early monitoring objective. [1,2,5,11]

2.2 Reproducible image acquisition and calibration protocol for an ordinary camera system

Because the pipeline uses a smartphone camera and flashlight, and compares repeated photographs over time, acquisition must control camera response, geometry, and illumination. The protocol below is designed to be reproducible on commodity devices while remaining practical at bedside.

Device specifications: For each deployment, use one fixed smartphone model and the rear wide camera module. Report the device model (for example, Apple iPhone 13 or Samsung Galaxy S22), operating system version, camera module, lens equivalent focal length, native resolution, and flash type. If multiple devices are used, calibrate each device separately and treat each device as a domain variable during model training and evaluation.

Capture mode and settings: RAW capture (DNG). Disable high dynamic range (HDR), beautification, auto scene optimization, and any dynamic tone mapping. Lock focus, exposure, and white balance after framing the region of interest. Fix International Organization for Standardization (ISO) (with the lowest non-boosted ISO number), fix shutter time to avoid saturation, fix focus distance (or tap-to-focus and lock), and fix white balance using a gray card reference captured under the same illumination.

Calibration procedure: At the start of each imaging session, capture (a) a gray card (18 percent) and (b) a color calibration target (e.g., ColorChecker) under the same illumination and geometry. Compute per-channel gains to map the captured gray patch to a neutral reference, then apply the same gains to sample images from that session. Estimate a 3 × 3 color correction matrix from the ColorChecker patches to reduce device-specific color bias. Remove vignetting by dividing by a precomputed flat-field image (captured from a uniform matte surface). Store calibration parameters with each session to support exact reproduction.

Quality control and logging: Reject images with saturation (clipped highlights), motion blur, or strong specular reflection. Log timestamp, device identifier, exposure settings (ISO, shutter, aperture if available), white balance gains, distance, and whether flash was used. These logs, together with the calibration targets, define a reproducible acquisition record. Note that this study involves only sample and simulated data, and clinical verification will be conducted in the future.

MCML simulations are performed offline to construct the ground-truth spectral database and to support DGM recalibration; in deployment, the trained CNN (with optional VDSR enhancement) performs per-image inference.

2.3 Chromophore variables used for ulcer risk prediction and the alert rule

Decision variables: Ulcer risk prediction is driven by two dermal-layer chromophore variables that reflect the primary pathophysiology of pressure injury: (i) dermal oxygenated Hb (HbO_2) as a proxy for local oxygenation and (ii) dermal water content as a proxy for edema. Other estimated variables (deoxygenated Hb, melanin, sebum, and optical parameters g, n, and d) are used for internal consistency checks and validation (e.g., to detect lighting artifacts or implausible parameter combinations) rather than for the alert decision.

We propose a complete operational process designed to assist healthcare professionals in the early detection and prevention of pressure ulcers through precise predictions and the analysis of internal skin parameters (Fig. 1). The process begins with photograph collection and input, where possible skin surface images are captured and input into the system as RGB data. In the spectral model analysis stage, the RGB data is converted into appearance optical property (AOP), which is then processed using the bio-optical model (BOM) to estimate the concentrations

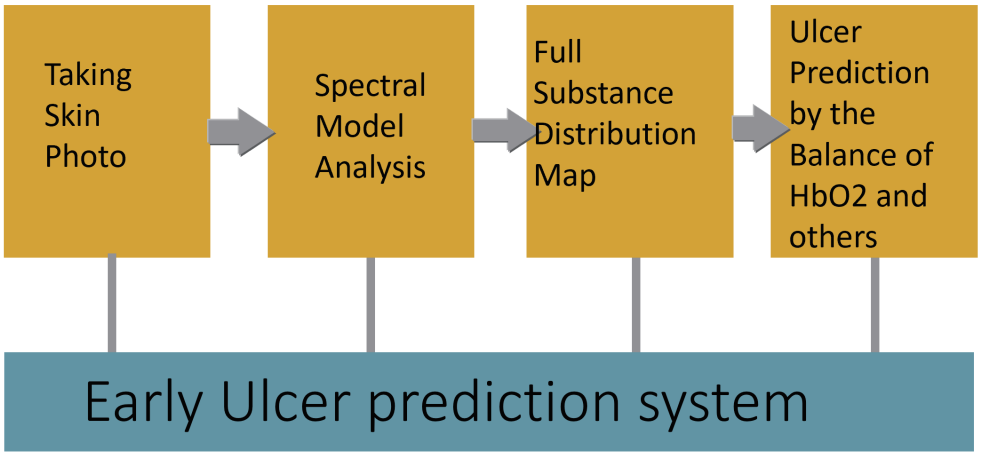

Fig. 1. (Color online) Flow chart of early ulcer prediction.

of oxygenated Hb, deoxygenated Hb, and water within the skin. The system then generates distribution maps and concentration predictions, displaying the internal concentrations of oxygenated Hb, deoxygenated Hb, and water in the skin tissue. These maps are analyzed to identify trends and predict future distributions, which can help pinpoint potential areas at risk for pressure ulcer formation. Finally, using the analysis results, the system produces an early pressure ulcer prediction and alert report, notifying healthcare professionals to enable timely preventive actions.

The hyperspectral model developed in this study can instantly analyze the concentration distribution of various chromophores in the skin tissues. The research methodology and execution in this study (Fig. 2) involve two key techniques. The double-end generative matching (DGM) technique (Fig. 2) is used for forward optical modeling and inverse sampling recalibration. In other words, the actual AOP hyperspectral data of the skin are transformed into the BOM of the internal chromophores of the skin. We establish a model to match the hyperspectral AOP obtained from literature with the internal chromophore BOM parameters, producing a large dataset with ground truth (Fig. 2). Subsequently, the deep hyperplane assimilation (DHA) method is utilized to establish an accurate optical model of skin tissue (Fig. 2). A CNN training model is then applied to convert the AOP of real skin-tissue photographs into a BOM. This BOM is subsequently matched with the ground-truth training dataset derived from the MCML method to obtain the most similar BOM, thereby yielding the BOM of the actual skin-tissue chromophores. Hyperspectral change analysis experiments are also incorporated during the compression and decompression of skin arterial vessels to elucidate the dynamic hyperspectral alterations in skin tissue resulting from changes in Hb content.

In this study, the DGM and DHA techniques (Fig. 2) are employed to accurately determine chromophore concentrations in skin tissue using forward optical modeling and inverse sampling recalibration. Surface spectra are first simulated via the MCML method using bio-optical parameters (g, n, d, μ_a, and μ_s) for each skin layer (Table 1)[27] and chromophore-related

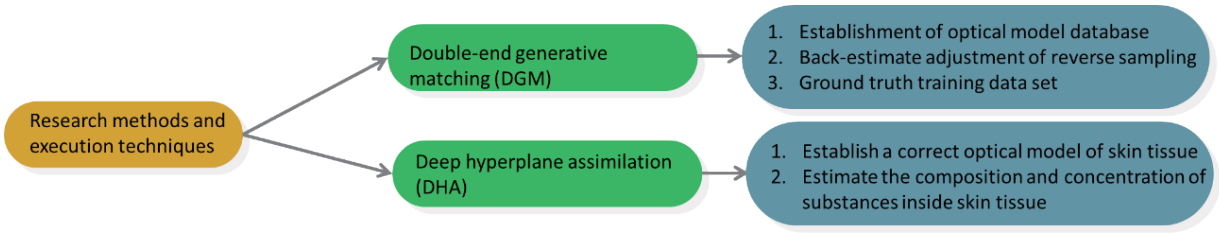

Fig. 2. (Color online) Research methods and execution techniques.

Table 1
Model of biological optical parameters of skin tissues.[27] Units: μ_a and μ_s are in mm^{-1}, d is in mm, and n and g are unitless.

Structure	n	μ_a	μ_s	g	d
Stratum corneum	1.5	0.27	108.1	0.88	0.0015
Epidermis	1.34	11.725	256.7	0.82	0.0075
Dermis	1.394	0.348	2213.33	0.92	0.1

physiological parameters (Table 2).[28] Absorption coefficients for water, oil, melanin, HbO_2, and Hb within the 400–720 nm range are derived from Monte Carlo tissue-scattering models. Photon and sampling settings are defined to generate large-scale surface spectral data for ground truth. Simultaneously, real skin images are used for reverse calibration, aligning simulated and observed spectral changes over time. This bidirectional matching process (Fig. 2) creates a spectral database enabling accurate chromophore quantification.

The optical model is refined through DHA using a deep CNN[29] and image enhancement via the very-deep super-resolution (VDSR) module (Fig. 2).[30] The spectral image module standardizes image formats, enabling training from RGB inputs through AOP to BOM outputs (Fig. 3). Deep learning reveals that each chromophore exhibits unique wavelength-dependent absorption, allowing GPU-accelerated simulations to predict AOP from chromophore concentrations in each skin layer. This framework enables the accurate estimation of the chromophore composition and distribution directly from skin photographs.

3. Results and Discussion

3.1 Generation of large training datasets with ground truth using DGM

Dataset generation details: The DGM training database is generated by sweeping the physiological parameter ranges in Table 2 together with the layer optical parameters in Table 1 and simulating surface reflectance spectra with MCML over 400–720 nm at 10 nm interval (33 bands). Each simulated spectrum is paired with its ground-truth BOM parameters. After augmentation, a supervised dataset with samples numbering on the order of 10^5–10^6 is typically sufficient for stable CNN training. The simulation dataset described in Sect. 2.1 provides paired RGB and spectrometer measurements for validation and DGM recalibration.

Table 2
Parameters used to calculate the absorption coefficients of the blood-containing layers of the skin. This table shows the data obtained from multiple sources, such as those indicated by Meglinski and Matcher.[28] Parameter conventions: $C_{melanin}$, C_{lipid}, and C_{blood} denote volume fractions (0–1); S denotes blood oxygen saturation (0–1); H_t denotes hematocrit (0–1); F_{Hb} and F_{RBC} are scaling fractions as defined by Meglinski and Matcher.[28]

Structure	$C_{melanin}$	C_{lipid}	C_{H_2O}	C_{blood}	S	H_t	F_{Hb}	F_{RBC}
Stratum corneum	0.1	0.2	0.05	0	0	0	0	0
Epidermis	0.03	0.151	0.2	0	0	0	0	0
Dermis	0	0.1733	0.5–0.7	0.15	0.6	0.45	0.99	0.25

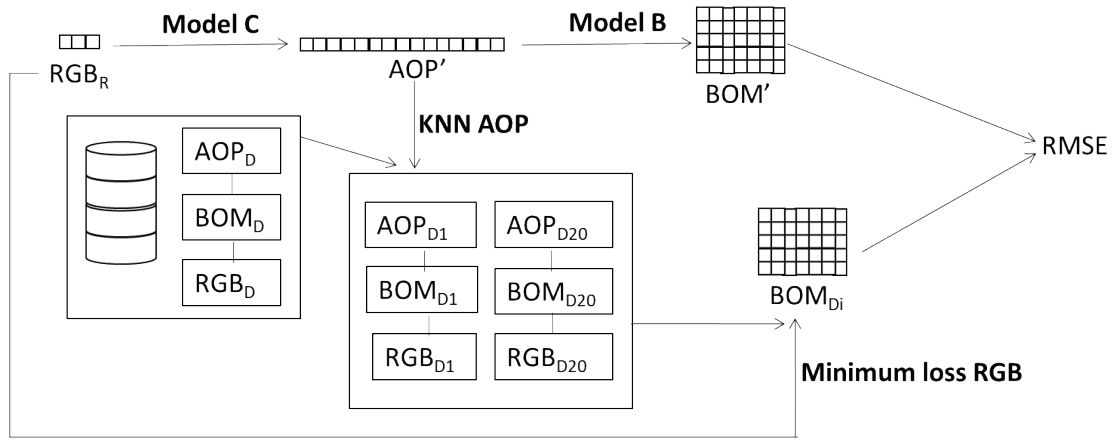

Fig. 3. Skin-texture optical-model training and verification for estimating internal skin tissue parameters (BOM). The top left corner, labeled RGB_R, represents the RGB image data obtained from the skin surface. This data is converted into the predicted AOP, denoted as AOP', using Model C. Then, a supervised machine learning algorithm selects the combination of AOP, BOM, and RGB from the database that most closely matches RGB_R, labeling them as AOP_D, BOM_D, and RGB_D, respectively. In this context, $AOP_{D1\sim20}$ refers to the AOP values corresponding to different BOMs, $BOM_{D1\sim20}$ represents various BOM combinations, and $RGB_{D1\sim20}$ contains the associated RGB data. Using Model B, AOP' is converted into BOM'. The correctly matching BOM_{Di} is then selected by calculating the minimum loss between RGB_R and RGB_D. Finally, the root mean square error (RMSE) between BOM' and BOM_{Di} is calculated to assess the accuracy of the prediction.

Adjusted tissue optical parameters are used to align predicted AOP spectra more closely with actual skin tissue spectra, forming the basis for a skin-tissue model training database. A substantial amount of ground truth data is required to train an accurate optical machine learning model. To address this, the smartphone-based remote multispectral photoplethysmography (SP-rmPPG) method used by He *et al.*[11] is referenced for monitoring spatial and temporal variations in HbO_2 and Hb using a smartphone camera and flashlight. In this study, facial skin images and reflectance data from a 45-year-old male are collected via smartphone and spectrometer as reference values for the DGM-based high spectral data. Three parameter sets are incorporated: (1) skin-tissue bio-optical properties (g, n, d, μ_a, and μ_s), (2) concentrations of water, sebum, melanin, HbO_2, and Hb across skin layers, and (3) chromophore absorption coefficients within

the 400–720 nm range, derived from Monte Carlo simulations. To reduce discrepancies between the predicted and actual spectra, simulation parameters are iteratively refined. Finally, data augmentation following the method of Shetty *et al.*[10] is applied using MCML to expand the training dataset and further improve the skin-tissue spectral prediction model. The current study protocol was approved by the Institutional Review Board of Kaohsiung Medical University (approval number: KMUHIRB-E(I)-20250118).

3.2 Establishment of skin-tissue spectral model and prediction and comparison of BOMs in skin tissue

Large-surface spectral data are validated using ground truth from extensive MCML simulations and an optical skin-tissue model developed via DGM and DHA deep learning, accurately representing the skin's BOM composition. Reflectance spectra (400–720 nm) from a 45-year-old male were divided into 33 segments (10 nm intervals), and discrepancies in AOP and BOM between the real and predicted data were analyzed. While AOP values showed notable differences (Fig. 4), likely owing to limitations in the training dataset, BOM comparisons revealed minimal deviations, confirming the model's reliability in predicting skin chromophore concentrations. The model's performance was further assessed by comparing the real BOM

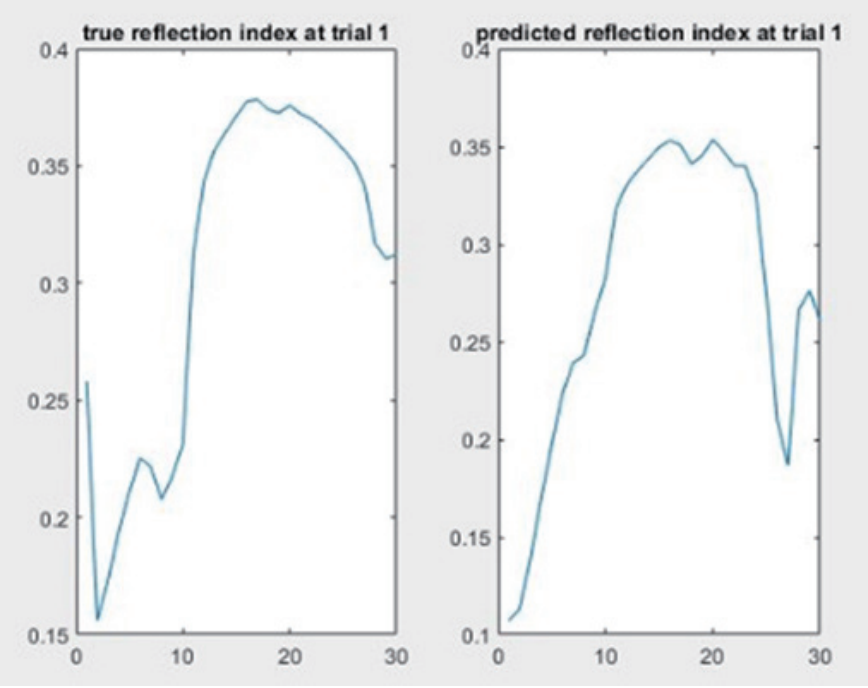

Fig. 4. (Color online) Hyperspectral-reflection differences between real and predicted skin tissues. To validate our optical model, we compare the AOP reflectance spectra of the real skin and the optical model predictions for a 45-year-old male. The spectral features in the 400–720 nm range are divided into 33 segments, each with a 10 nm interval, to compare the AOP values. Significant differences are observed between the real and predicted AOP values, possibly because of the relatively limited training dataset currently available.

(BOMr) and predicted BOM after CNN training (BOMrm) across skin layers, including HbO_2, Hb, water, fat, melanin, g, d, and n. The high consistency between BOMr and BOMrm (Table 3) demonstrates the model's accuracy in chromophore prediction.

Quantitative discrepancy metrics for Fig. 4: In addition to the visual spectral plot, we report compact error metrics computed over the 33 wavelength bands. Let r_i and p_i denote the real and predicted reflectances at band i, respectively. We compute RMSE, MAE, and the spectral angle mapper (SAM).

3.3 Chromophore concentration distributions in tissues obtained using pressure ulcer photos

Our findings successfully demonstrate that the established hyperspectral model can be applied to analyze chromophore concentration distributions within skin tissues using skin photos. Results reveal that deoxygenated Hb and HbO_2 are predominantly concentrated in the dermis, water content is higher in the dermis than in the epidermis, melanin is concentrated in the epidermis, and fat accumulates in the subcutaneous tissue. These phenomena are consistent with actual skin conditions. The hyperspectral model developed in this study can accurately predict the concentration and distribution of chromophores in skin tissues (Fig. 5, Table 4), enabling the early warning of pressure ulcers.

Predicted concentrations of deoxygenated Hb and HbO_2 are highest in the dermis (5.46×10^{-3}/8.7×10^{-1}), with significantly lower values in the stratum corneum (9.10×10^{-6}/7.96×10^{-7}) and epidermis (3.96×10^{-6}/1.95×10^{-6}), consistent with the findings of Meglinski,[31] who also report elevated HbO_2 levels in the dermis (0.04–0.14) and negligible HbO_2 levels in upper layers (Fig. 5). The results of this study confirm that both oxygenated Hb and

Table 3
BOM_r of real skin in different tissue layers, AOP_r, and differences in BOM_{rm} obtained after CNN training. Using the established skin tissue spectral model, we compare the actual BOM (BOM_r) with the CNN-trained BOM (BOM_{rm}). The experiment evaluates the concentrations of HbO_2, Hb, water, fat, melanin, *g*, *d*, and *n* in the stratum corneum, epidermis, and dermis. The results show that both datasets are highly similar, demonstrating that the model can accurately predict the concentrations of various chromophores in different skin layers.

Chromophores	Structure					
	Stratum corneum		Epidermis		Dermis	
	BOM_r^*	BOM_{rm}^{δ}	BOM_r^*	BOM_{rm}^{δ}	BOM_r^*	BOM_{rm}^{δ}
HbO_2 (%)	0	0	0	0	84.22	82.89
Hb (%)	0	0	0	0	0	0
Water (%)	18.72	18.83	64.39	63.97	65.81	61.18
Sebum (%)	9.99	9.97	9.99	9.97	19.99	19.94
Melanin (%)	9.99	9.97	0	0	0	0
g	0.8995	0.8974	0.7995	0.7997	0.8995	0.8974
d (mm)	1.5×10^{-3}	1.5×10^{-3}	7.5×10^{-3}	7.5×10^{-3}	9.99×10^{-2}	9.97×10^{-2}
n	1.4991	1.4956	1.2992	1.2962	1.3992	1.3959

Note *: BOM converted from AOP of real skin; $^{\delta}$: BOM obtained from AOP of real skin after CNN training.

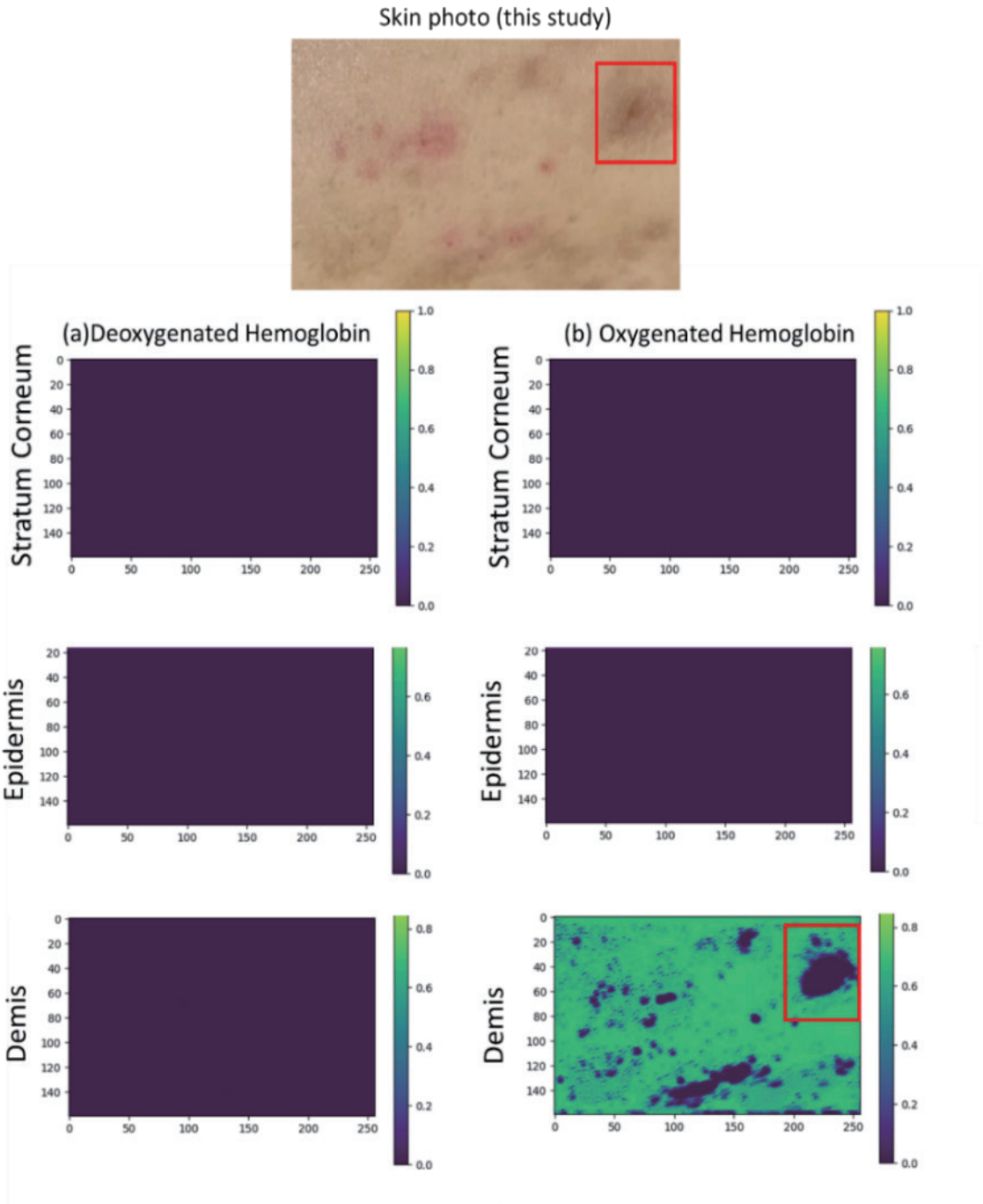

Fig. 5. (Color online) Concentrations and distributions of chromophores within skin tissues predicted by the developed hyperspectral model. (a) Deoxygenated Hb. (b) Oxygenated Hb. We obtained a photo of a skin sample from a pressure ulcer from the internet (the top picture) to predict the oxygenated Hb and deoxygenated Hb concentrations in the stratum corneum, epidermis, and dermis. The results show that oxygenated Hb and deoxygenated Hb are primarily concentrated in the dermis, with lower levels of oxygenated Hb at the pressure ulcer site (highlighted in the red box) than in the surrounding tissue.

Table 4
Predicted average concentrations of chromophores in skin tissue using the developed hyperspectral model. Units: All entries are reported as dimensionless fractions (0–1) within each layer; small values are shown in scientific notation using $\times 10^{k}$ for clarity.

Structure	Chromophores			
	Deoxygenated Hb	Oxygenated Hb	Water	Melanin
Stratum corneum	9.10×10^{-6}	7.96×10^{-7}	0.090684	0.0300
Epidermis	3.96×10^{-6}	1.95×10^{-6}	0.538565	0.004147
Dermis	5.46×10^{-3}	0.87078	0.481218	2.17×10^{-7}

Note: This table presents the predicted average concentrations of deoxygenated Hb, oxygenated Hb, water, and melanin in the stratum corneum, epidermis, and dermis layers obtained using the developed hyperspectral model. These predictions are compared with findings from previous studies. The results indicate that the dermis contains higher levels of HbO_2 than the stratum corneum and epidermis.

deoxygenated Hb are concentrated in the dermis, and that oxyhemoglobin levels are reduced at pressure ulcer sites compared with surrounding tissue.

The predicted water content in the stratum corneum (0.09), epidermis (0.538), and dermis (0.48) closely matches theoretical values (0.05, 0.2, and 0.5–0.7) from prior studies,[31] reaffirming the trend of increasing hydration with skin depth.

Predicted melanin concentrations (2.17×10^{-7}–3.0×10^{-2}) align with theoretical ranges (0–0.1),[31] with minimal variation due to pressure ulcers being observed. Future work will focus on the HSI of subclinical skin tissue changes, with the aim of establishing a real-time, dynamic prediction system for monitoring skin circulatory health.

4. Conclusions

The discrepancies between the predicted and actual reflectance spectra of various chromophore BOMs across different skin layers (stratum corneum, epidermis, and dermis) were minimal. This demonstrates our model's ability to predict chromophore concentrations accurately. In this study, by developing a precise spectral model of skin tissue, we were able to derive the distribution of oxyhemoglobin, deoxyhemoglobin, and water within the skin from an arbitrary photograph. This enabled the identification of areas in the dermis with low levels of oxygenated Hb and abnormal water content, which will help prevent skin tissue damage and inhibit pressure ulcer formation.

Our model decomposes a complete set of contents into skin layers using an arbitrary picture. Although only two substances are deterministic to the prediction of ulcers, the results for the rest of the substances validate the consistency of our estimation. Our results show consistency between our prediction and the ground truth. The pressure ulcer prediction system's operational process designed in this study allows healthcare professionals to prevent pressure ulcers and implement preventive measures in advance.

Acknowledgments

This work was supported by the National Science and Technology Council, Taiwan, under Grants no. MOST 110-2622-E-992-026 and NSTC 112-2221-E-037-004-MY3. The authors also thank Yuan's General Hospital (ST111007), NKUST-KMU joint research project (Grant no. NKUSTKMU-112-KK-009), NSYSU-KMU joint research project (Grant no. NSYSU-KMU-114-P06), and Kaohsiung Medical University (KMU-TC115A06-1), Kaohsiung 807, Taiwan.

References

1 M. Nouvong, B. Hoogwerf, E. Mohler, B. Davis, and A. Tajaddini: Diabetes Care **32** (2009) 2056. https://doi.org/10.2337/dc09-0313
2 D. Kapsokalyvas, N. Bruscino, D. Alfieri, V. de Giorgi, G. Cannarozzo, R. Cicchi, D. Massi, N. Pimpinelli, and F. S. Pavone: Opt. Express **21** (2013) 4826. https://doi.org/10.1364/OE.21.004826
3 D. Jakovels, J. Spigulis, and I. Saknite: Proc. SPIE (2010) 7715. https://doi.org/10.1117/12.853928
4 Q. He and R. Wang: Biomed. Opt. Express **11** (2020) 895. https://doi.org/10.1364/BOE.378470
5 T. Bydlon, R. Nachabe, N. Ramanujam, H. Sterenborg, and B. Hendriks: J. Biophotonics **8** (2015) 9. https://doi.org/10.1002/jbio.201300198
6 E. Salomatina, B. Jiang, J. Novak, and A. N. Yaroslavsky: J. Biomed. Opt. **11** (2006) 064026. https://doi:10.1117/1.2398928
7 G. N. Stamatas and N. Kollias: J. Biomed. Opt. **12** (2007) 051603. https://doi:10.1117/1.2798704
8 G. Zonios, A. Dimou, I. Bassukas, D. Galaris, A. Tsolakidis, and E. Kaxiras: J. Biomed. Opt. **13** (2008) 014017. https://doi:10.1117/1.2844710
9 J. Wu: Photodiagn. Photodyn. Ther. **45** (2024) 104003. https://doi:10.1016/j.pdpdt.2024.104003
10 B. Shetty, R. Fernandes, A. P. Rodrigues, R. Chengoden, S. Bhattacharya, and K. Lakshmanna: Sci. Rep. **12** (2022) 18134. https://doi:10.1038/s41598-022-22644-9
11 Q. He, Z. Sun, Y. Li, W. Wang, and R. K. Wang: Biomed. Opt. Express **12** (2021) 2919. https://doi:10.1364/BOE.423160
12 S. Kazune, C. Anastasija, L. Einars, V. Karina, and G. Andris: Ann. Intensive Care **9** (2019) 97. https://doi:10.1186/s13613-019-0572-1
13 B. Khoobehi, M. B. James, and K. Hiroyuki: IOVS **45** (2004) 1464. https://doi:10.1167/iovs.03-1069
14 I. Ahmed, M. Ali, and H. Butt: Micromachines **14** (2023) 955. https://doi: 10.3390/mi14101955
15 E. Drakaki and I. Sianoudis: e-J. Sci. Technol. (eJST) **3** (2008) 1.
16 M. Shimada, Y. Masuda, Y. Yamada, M. Itoh, M. Takahashi, and T. Yatagai: Opt. Rev. **7** (2000) 348. https://doi:10.1007/s10043-000-0348-7
17 M. Shimada, Y. Yamada, M. Itoh, and T. Yatagai: Phys. Med. Biol. **46** (2001) 2385. https://doi:10.1088/0031-9155/46/9/308
18 N. Tsumura, H. Haneishi, and Y. Miyake: J. Optical Soc. America A **16** (1999) 2169. https://doi:10.1364/JOSAA.16.002169
19 C. Magnain, M. Elias, and J. Frigerio: J. Optical Soc. America A **24** (2007) 2196. https://doi:10.1364/JOSAA.24.002196
20 C. Magnain, M. Elias, and J. Frigerio: J. Optical Soc. America A **25** (2008) 1737. https://doi:10.1364/JOSAA.25.001737
21 R. Ohtsuki, S. Tominaga, and O. Tanno: Opt. Rev. **19** (2012) 254. https://doi:10.1007/s10043-012-0039-1
22 R. N. Jadoon, A. Shahzad, S. A. A. Shah, M. A. Khan, T. Akram, and W. Zhou: Appl. Sci. **10** (2020) 8238. https://doi:10.3390/app10228238
23 A. Moco, S. Stuijk, and G. de Haan: Sci. Rep. **8** (2018) 8501. https://doi:10.1038/s41598-018-26068-2
24 L. Wang, S. L. Jacques, and L. Zheng: Comput. Methods Programs Biomed. **47** (1995) 131. https://doi:10.1016/0169-2607(95)01640-F
25 A. Doronin and I. Meglinski: Biomed. Opt. Express **2** (2011) 2461. https://doi:10.1364/BOE.2.002461
26 A. Doronin and I. Meglinski: J. Biomed. Opt. **17** (2012) 0905041. https://doi:10.1117/1.JBO.17.9.090504
27 K. Das, Y. Tomonori, N. Izumi, F. Hideki, and A. Yoshihisa: Opt. Rev. **27** (2020) 233. https://doi:10.1007/s10043-020-00579-8

28 I. V. Meglinski and S. J. Matcher: Comput. Methods Programs Biomed. **70** (2003) 179. https://doi:10.1016/s0169-2607(02)00099-8
29 X. Li, J. S. J. Ren, C. Liu, and J. Jia: Proc. 28th Int. Conf. Neural Information Processing Systems **1** (2014) 1790. https://dl.acm.org/doi/proceedings/10.5555/2968826
30 Very-Deep Super-Resolution (VDSR). https://www.mathworks.com/help/images/single-image-super-resolution-using-deep-learning.html
31 I. Meglinski: Quantum Electron. **31** (2001) 1101. https://doi:10.1070/QE2001v031n12ABEH002108